Melanin inspired microcapsules delivering immune metabolites for hepatic fibrosis management

Xin Zhao, Zun Fan, Chengyang Zhu, Weigang Zhang [**], Lei Qin [*]

Department of General Surgery, The First Affiliated Hospital of Soochow University, Suzhou, 215006, China

ABSTRACT

Patients with hepatic fibrosis (HF) have a high risk of developing liver cirrhosis and hepatocellular carcinoma, and there is an urgent need for preventive strategies to block this process. Previous studies have found that disordered inflammation and oxidative damage play important roles in HF progression, suggesting two attractive therapeutic targets. Herein, a new kind of bioinspired microcapsules with a core-shell structure is generated using microfluidics. Polydopamine nanoparticles (PDANPs), a synthetic analogue of natural melanin, are embedded in the polymer shell to provide antioxidative properties for these microcapsules. The aqueous core is used to encapsulate ketone body β-hydroxybutyrate (BHB), an energy metabolite recently known to have regulating effects of cellular signals involved in chronic inflammation. In a HF mouse model, the BHB-encapsulated PDANPs-embedded microcapsules (BHB-PDA-MCs) can not only decrease the severity of inflammatory response, but also the level of oxidative stress. As a result, this combinational strategy is demonstrated to prevent the activation of hepatic stellate cells, the accumulation of extracellular matrix, and the damage of hepatic lobules. These findings indicate that BHB-PDA-MCs can be a promising drug delivery system and have a synergistic effect on HF management.

1. Introduction

Hepatic fibrosis (HF) is a global health problem characterized by excessive accumulation of extracellular matrix (ECM) proteins in the liver [1]. Chronic liver injuries from any etiology can lead to HF, mainly including hepatitis B and/or hepatitis C infections, alcoholic liver diseases, non-alcoholic steatohepatitis, autoimmune and biliary diseases [2]. Without effective interventions, advanced HF will disrupt the normal hepatic architecture and function, and progress to cirrhosis, an end-stage consequence causing life-threatening complications of portal hypertension and liver failure [3]. In addition, patients undergoing HF also have a high risk to develop hepatocellular carcinoma (HCC) [4]. Fortunately, many clinical studies and experimental rodent models have demonstrated that HF is a highly dynamic and reversible process, which means that therapeutic strategies can be designed to facilitate fibrosis resolution [5].

Although the exact mechanism of HF has not been completely understood, chronic inflammation is now considered as a driving force in disease progression [6]. Following tissue damage, the activation of liver-resident macrophages as well as the recruitment of peripheral

leukocytes contributes to inflammatory cascades by releasing a large variety of bioactive factors. If the inflammation fails to resolve and develops into a chronic state, these persistent factors will act as intracellular signaling mediators to promote the *trans*-differentiation of quiescent hepatic stellate cells (HSCs) into proliferative myofibroblasts. These activated HSCs express α-smooth muscle actin (α-SMA), develop contractile function, synthesize ECM components abundantly, and disrupt the normal architecture of liver lobules [7]. Recently, NLRP3 inflammasome, a cytoplasmic multiprotein complex, has been shown to control the release of bioactive factors in local and invading immune cells [8]. It is an important innate immune sensor that can be triggered by a variety of stimuli, such as infection, tissue damage, and metabolic dysregulation. Emerging evidences have demonstrated that the inhibitors of NLRP3 inflammasome are beneficial for hindering the disease progression of HF [9]. On the other hand, it has long been postulated that oxidative environment also participates in the development of HF patients [10]. During inflammatory episodes, reactive oxygen species (ROS) were released in excess from the activated immune cells. Meanwhile, the activity of antioxidative enzymes is also inhibited, leading to the alteration of redox equilibrium and oxidative damage of hepatocytes [11]. In addition, ROS

---

can act both as an inflammatory molecule and a signaling mediator to further activate the immune cells and promote the *trans*-differentiation of HSCs directly [12]. Resultantly, the mutual deterioration caused by chronic inflammation and oxidative stress accelerates the deposition of ECM proteins and damage of hepatic lobules, and contributes to the formation of liver cirrhosis and HCC in HF patients. Therefore, targeting the inflammatory response and scavenging ROS may be efficient strategies to attenuate HF development.

The ketone body β-hydroxybutyrate (BHB) is produced by fatty acid β-oxidation in the liver and serves as an alternative energy source during nutrient deprivation [13]. Strikingly, BHB is also demonstrated to be a kind of regulatory metabolites, and possesses of important cellular signaling functions by acting as an inhibitor to control the priming and assembly of NLRP3 inflammasome [14]. Recent studies have reported that the NLRP3-targeted effects of BHB can function as a key immune-metabolic checkpoint, and have protective effects in a range of inflammation-induced diseases, such as ulcerative colitis, gouty arthritis, atherosclerosis, and chronic heart failure [13–15]. However, whether exogenous supplement of BHB provides a therapeutic strategy for HF remains to be proved. Another noteworthy point is that direct administration of water-soluble BHB is insufficient to achieve effective concentration owing to the rapid clearance [16]. In this study, microcapsules with a unique core-shell structure were prepared to serve as drug delivery systems for BHB. Microencapsulation of drug molecules is an effective way of enhancing their biological activities, reducing side effects on the host organs, and preventing possible interaction with the surroundings and leakage during the fabricating process. Based on the tailorable microstructures and surface chemistry, microcapsules also allow modulating the release profiles of encapsulated cargos, offering unique advantages in controlled drug delivery [17]. In addition, the high flexibility of material selection for engineering the shell enables production of microcapsules with biocompatibility, biostability, biodegradability, and multifunctionality [18].

Here, a simple microfluidic approach is employed to generate a new kind of bioinspired microcapsules for controlled delivery of BHB, with the shell composed of poly(lactic-co-glycolic acid) (PLGA) and polydopamine nanoparticles (PDANPs) (Fig. 1). PDANPs are a synthetic analogue of natural melanin pigment, produced from polymerization of dopamine molecules under alkaline conditions. Because of the cell-adhesive property, antibacterial activity, and satisfied biocompatibility, PDANPs have attracted considerable attentions in the fields of biomedicine [19]. In addition, PDANPs are demonstrated to have ROS scavenging ability based on the abundant reductive functional groups on their surface [20]. However, the incorporation of PDANPs into microcapsules as a robust antioxidant to prevent oxidative stress-involved tissue damage has not yet been reported to the best of our knowledge. Based on the above descriptions, the polydopamine-embedded microcapsules (PDA-MCs) with BHB encapsulation (BHB-PDA-MCs) are speculated to have both anti-inflammatory and antioxidative effects, because of the NLRP3 inflammasome-inhibited activity of BHB and ROS scavenging ability of PDANPs. The in vitro experiments showed that PDANPs embedded in the polymer shell could alleviate the oxidative levels in hepatocytes and HSCs stimulated by H_2O_2, while BHB released from the aqueous core could reduce the production of pro-inflammatory and pro-fibrotic factors from macrophages. Finally, whether the dual regulation effects of BHB-PDA-MCs have a protective role in HF progression was evaluated in mice models induced by carbon tetrachloride (CCl_4). The in vivo results showed that BHB-PDA-MCs could inhibit HSCs activation, reduce ECM proteins deposition, and attenuate hepatic lobules disruption. Together, these features indicate that the proposed BHB-PDA-MCs possess of promising potentials in HF management.

2. Results and discussion

In this experiment, PDANPs were first synthesized via the self-polymerization approach of dopamine monomer under alkaline condition at room temperature. The transmission electron microscope (TEM) image of PDANPs showed that they had a relatively uniform morphology with an average diameter of about 390 nm (Fig. 2a). When compared with the ^{1}H nuclear magnetic resonance (NMR) spectrum of dopamine monomer and PDANPs in deuterium oxide (D_2O) system, no detectable proton signals of dopamine monomer were found in PDANPs, indicating the excellent stability of PDANPs without any depolymerization (Fig. S1). Then, the double emulsion-templated BHB-PDA-MCs were fabricated using a capillary microfluidic device, which was assembled by aligning three cylindrical capillaries (inner, middle, and outer capillaries) coaxially inside a square capillary. BHB dissolved in deionized water was used as the inner aqueous phase and pumped into the inner capillary. PDANPs
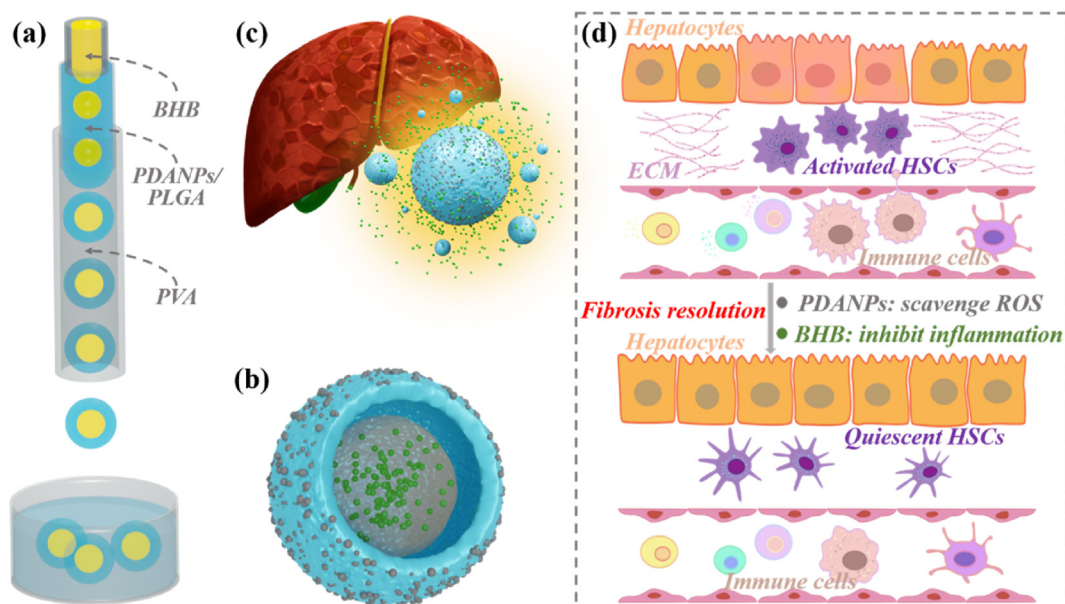

Fig. 1. a) Schematic diagram of BHB-PDA-MCs fabrication from microfluidic double emulsion templates. b) Schematic diagram of BHB-PDA-MCs with a core-shell structure. c) Schematic diagram of BHB-PDA-MCs in application of HF management. d) Mechanism diagram showed that BHB-PDA-MCs prevented HSCs activation and ECM deposition by PDANPs-mediated ROS scavenging and BHB-mediated inflammatory inhibition.
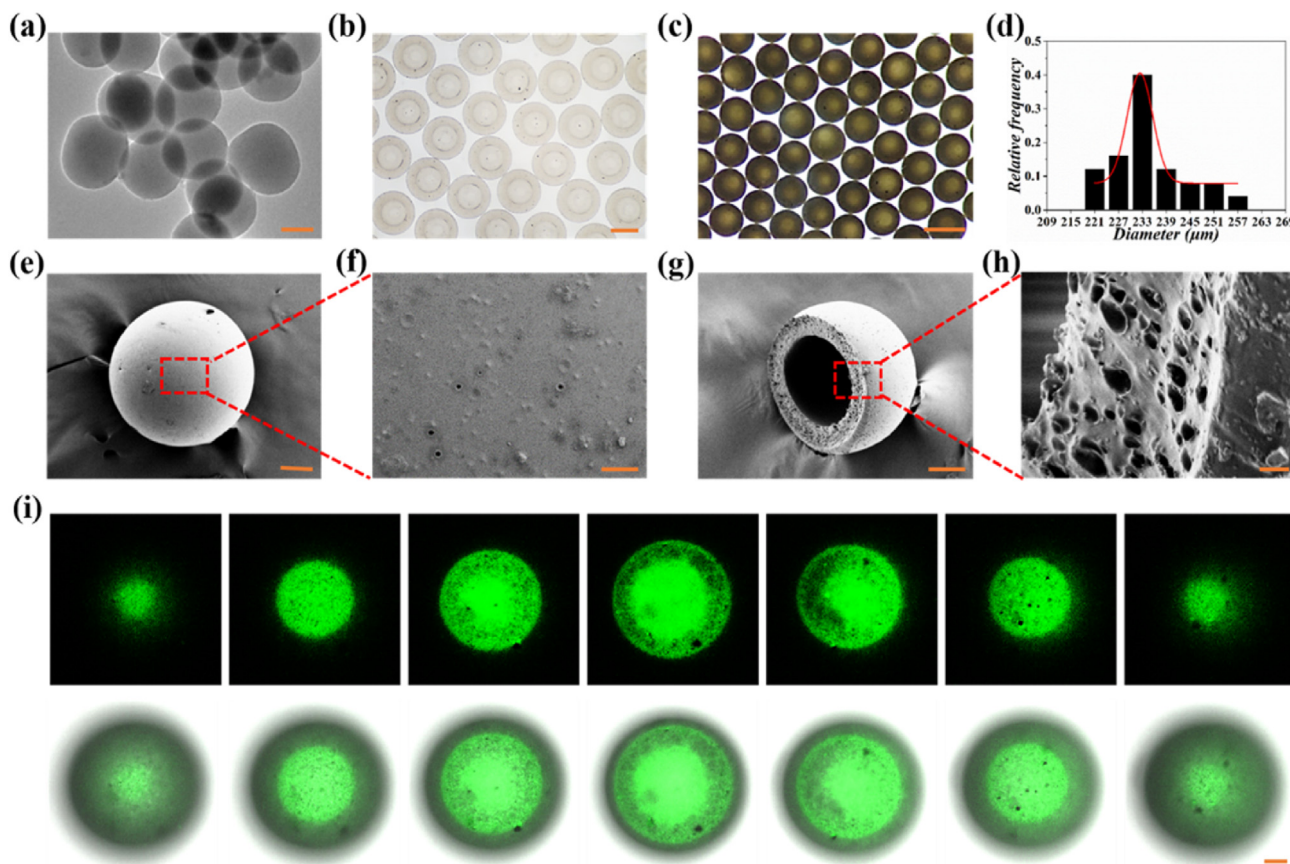
Fig. 2. a) TEM image of PDANPs. b) Optical microscope image of W/O/W double emulsions. c) Optical microscope image of BHB-PDA-MCs. d) Statistical size distribution of BHB-PDA-MCs. e) SEM image of BHB-PDA-MCs from an external view. f) Magnified image of the rough surface in (e). g) SEM image of BHB-PDA-MCs from a cross-sectional view. h) Magnified image of the polymer shell in (g). i) Layer-by-layer confocal laser scanning images of FITC-PDA-MCs. The scale bars were 200 nm in (a), 250 μm in (b, c), 50 μm in (e, g, i), and 5 μm in (f, h).

dispersed in PLGA solution was used as the middle oil phase and pumped into the region between the inner and middle capillary. PVA solution, a surfactant, was used as the outer aqueous phase and pumped into the region between the middle and outer capillary. When these fluids flowed through the microfluidic device, aqueous cores containing BHB were generated at the tip of inner capillary and were subsequently encapsulated by a shell droplet of PDANPs/PLGA at the tip of middle capillary in a dripping mode (Fig. S2a). Benefited from the co-flow geometries of microfluidic device, symmetric shearing force was employed to generate double emulsion templates in a stable and controllable manner. As shown in Fig. 2b, the obtained water-in-oil-in-water (W/O/W) double emulsions exhibited high monodispersity, with the inner aqueous cores engulfed fully by the oil droplets of annular sheath in a radially symmetric pattern. The average diameters of inner cores and outer droplets were 266.66 μm and 537.06 μm, respectively, with the coefficient of variation (CV) value less than 5% (Figs. S2b and c). In addition, by regulating the flow rates of three phase fluids, double emulsions with multiple inner cores could also be generated with high uniformity (Figs. S2d–i), and the relationship between the flow rates of three phase fluids and the number of inner cores were described in Fig. S3. Therefore, the double emulsions generated by microfluidics could serve as satisfied templates for fabricating BHB-PDA-MCs.

As PDANPs/PLGA in the middle phase was dissolved in dichloromethane (DCM), a volatile organic solvent, the obtained double emulsion templates could be solidified after DCM evaporation. To achieve desired morphology and structure, high concentration of PLGA (>10%) should be employed to guarantee the rapid formation of polymer shell. As shown in Fig. 2c, the full shaped BHB-PDA-MCs were stable, different from

previously reported microcapsules with collapsed morphology [21]. Consistent with the original double emulsion templates, the fabricated BHB-PDA-MCs also had a high monodispersity (Fig. 2d), with the CV value of 4.53%. The detailed morphology and structure of BHB-PDA-MCs were observed under scanning electron microscope (SEM). From an external view, the microcapsules were standard spheres with an average diameter of about 230 μm (Fig. 2e). From a cross-sectional view, a hollow core surrounded by an intact shell was presented perfectly (Fig. 2g). Meanwhile, PDANPs were found to distribute across the polymer shell of microcapsules shown in the magnified images (Fig. 2f, h). To observe the drug storage in BHB-PDA-MCs, fluorescein isothiocyanate (FITC), instead of BHB, was encapsulated into the aqueous cores of microcapsules (FITC-PDA-MCs) and subjected to tomography scan using a confocal microscope. As shown in Fig. 2i, the green fluorescence emitted by FITC was confined to the aqueous cores of FITC-PDA-MCs, with little fluorescent signals diffusing into the polymer shells. Taken together, the uniform morphology and desired core-shell structure of BHB-PDA-MCs indicated their potential value in drug delivery systems.

Theoretically, the hollow cores of microcapsules provide much space for encapsulating bioactive molecules and considered to have a high drug loading efficiency. However, the hostile preparation process of traditional interfacial polymerization technology, layer-by-layer assembly approach, and electro-spraying strategy results in massive leakage of cargos during the fabrication of microcapsules, hindering their practical applications [22]. The mild emulsification process in microfluidic system provides a feasible solution to overcome the problem. As shown in Fig. 3a and b, the encapsulation efficiency and loading content of FITC-PDA-MCs were up to 79.92% and 1.07 μg/mg, respectively. On the other hand,
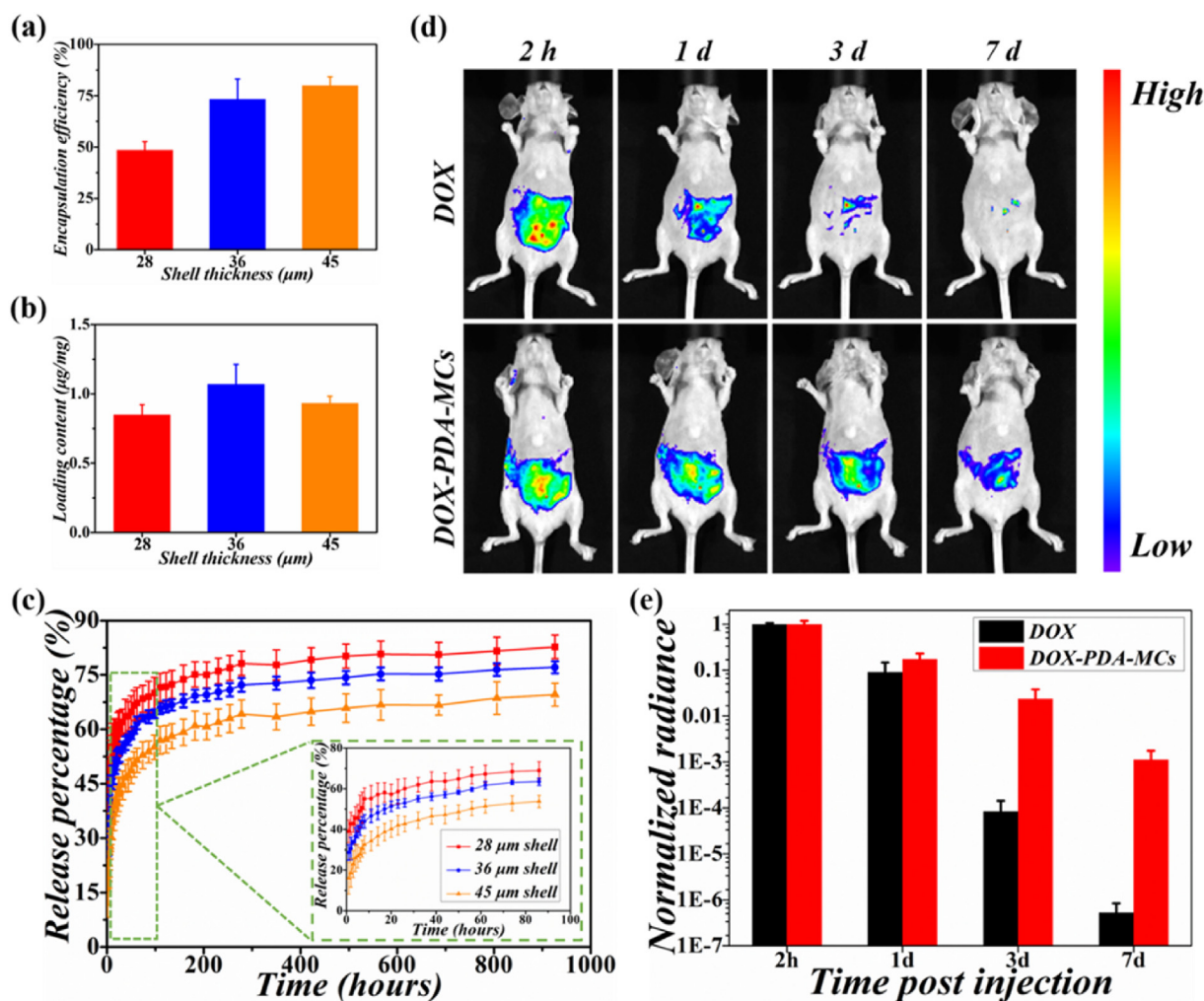
Fig. 3. a) Effects of the PLGA concentration on drug encapsulation efficiency of FITC-PDA-MCs. b) Effects of the PLGA concentration on drug loading content of FITC-PDA-MCs. c) In vitro accumulative drug release from FITC-PDA-MCs with different shell thickness, the inset showed the accumulative release of encapsulated drugs in the first 80 h. d) In vivo fluorescent images of nude mice injected with free DOX or DOX-PDA-MCs. e) Total radiance over time normalized to the initial 2 h signal of free DOX or DOX-PDA-MCs. Error bars represented standard deviations.

PLGA concentration is an important parameter that influences the drug loading efficiency of FITC-PDA-MCs. When 10% PLGA used, the polymer solidification was delayed with a shell thickness as low as 28 μm, and the fabricated FITC-PDA-MCs presented a collapsed appearance (Fig. S4a). All these disadvantages resulted in a poor encapsulation efficiency (48.48%) and loading content (0.85 μg/mg). In contrast, when 12% PLGA used, rapid polymer solidification was realized with a shell thickness of 36 μm, and the fabricated FITC-PDA-MCs presented a full shape (Fig. S4b). Accordingly, the encapsulation efficiency and loading content were dramatically improved to 73.23% and 1.07 μg/mg, respectively. When further increasing PLGA concentration to 15%, although the shell thickness reached 45 μm (Fig. S4c), the encapsulation efficiency (79.92%) and loading content (0.93 μg/mg) of FITC-PDA-MCs showed negligible changes.

Previous studies have reported that, for drug delivery systems based on microcapsules, the release of cargos entrapped in the core reservoir was realized by molecule diffusion through the polymer shell [18]. To evaluate the drug delivery performance of FITC-PDA-MCs under physiological conditions, these microcapsules were immersed into PBS solution at 37 °C and FITC release was monitored over time (Fig. 3c). Upon the immersion of FITC-PDA-MCs, FITC quickly diffused into PBS solution driven by concentration gradient and its cumulative release amount

increased remarkably over time. Taken FITC-PDA-MCs with 36 μm shell thickness as an example, an initial burst release of 46.64% FITC was observed within 10 h. Then, the concentration gradient inside and outside the polymer shell decreased gradually, resulted in a slow release of 30.45% FITC from 10th to 925th hour. As well known, the shell thickness plays a significant role in determining the drug delivery performance of microcapsules, three kinds of FITC-PDA-MCs with different shell thickness were immersed into PBS solution respectively to compare their release profiles. Not surprisingly, when the shell thickness was 28 μm, the rate of drug release was the fastest. With the shell thickness increased, the release process of FITC-PDA-MCs showed a more sustained pattern. As the polymer shell of microcapsules could serve as a diffusion barrier to limit drug delivery, the more tedious release from FITC-PDA-MCs with a thicker shell could be attributed to the longer distance before FITC contacted PBS solution [23]. In general, taking advantages of FITC-PDA-MCs, large amounts of drug molecules could be encapsulated into the hollow cores, and released in a controlled manner by regulating the shell thickness at different PLGA concentration.

For the treatment of chronic diseases like HF, the continuous drug release over several days is often essential. However, insufficient stability of traditional delivery systems may lead to premature leakage of entrapped drugs and influence their therapeutic performances [24]. In

contrast, the stability of microcapsules with an intact shell is expected to be adequate for long-term drug delivery in vivo. To evaluate the in vivo retention time of BHB-PDA-MCs, doxorubicin (DOX), instead of BHB, was encapsulated into the aqueous core of microcapsules (DOX-PDA-MCs) and subjected to fluorescent signal detection using an in vivo imaging system. As shown in Fig. 3d and Figs. S5 and 6, when free DOX injected into nude mice, the fluorescent signals decayed rapidly from 1-day post injection and was almost undetectable at 3-day post injection. In contrast, when DOX-PDA-MCs injected into nude mice, the fluorescent signals were much higher than free DOX from 1-day post injection, indicating that the decay rate was significantly slowed down. From the statistical analysis in Fig. 3e, it was shown that the normalized radiance of DOX-PDA-MCs group at 1-day post injection was 0.91-fold higher than free DOX group. In addition, this difference increased dramatically to 2.82×10^2-fold at 3-day and 2.15×10^3-fold at 7-day post injection. Then, the major organs of nude mice were collected at 3-day post injection of DOX-PDA-MCs and subjected to ex vivo fluorescent imaging. As shown in Fig. S7, the released DOX from microcapsules was widely distributed in the heart, liver, lung, and kidney. These results demonstrated that free drugs were metabolized and cleaned rapidly from the whole body with negligible dose left in mice after three days post injection, while microencapsulation prolonged the retention time of loaded

drugs to over seven days, leading to the enhancement of their bioactive functions in vivo.

As a melanin analogue, PDANPs have been regarded as a promising class of nanomaterials in biomedical fields because of their excellent biocompatibility and biodegradability, as well as unique antioxidative properties. Previous studies have found that the abundant phenolic hydroxyl groups presented on the surface of PDANPs can deplete various ROS including H_2O_2, $\cdot OH$, and $\cdot O_2^-$. In addition, compared with traditional antioxidants, such as coenzyme Q and vitamin C, the ordered nonplanar nanostructures of PDANPs make them exert a more stable antioxidative effect [19]. To investigate the antioxidative properties of PDA-MCs, free radical scavenging test was conducted via 2, 2-diphenyl-1-pyridinium hydrazine (DPPH) assay. As shown in Fig. S8, the free radical scavenging processes could be obviously observed by the apparent color disappearance of DPPH solution. The statistical results exhibited in Fig. 4c demonstrated that PDANPs incorporated into the polymer shell of microcapsules had a dose-dependent enhancement of antioxidative properties. The pure shell without PDANPs incorporation showed a negligible free radical scavenging ability. In contrast, the composite shell containing 0.5%, 1.0%, 1.5%, and 2.0% PDANPs cleared over 14.7%, 23.7%, 35.4%, and 42.2% of DPPH free radicals, respectively. Subsequently, the ability of PDA-MCs to relieve the oxidative
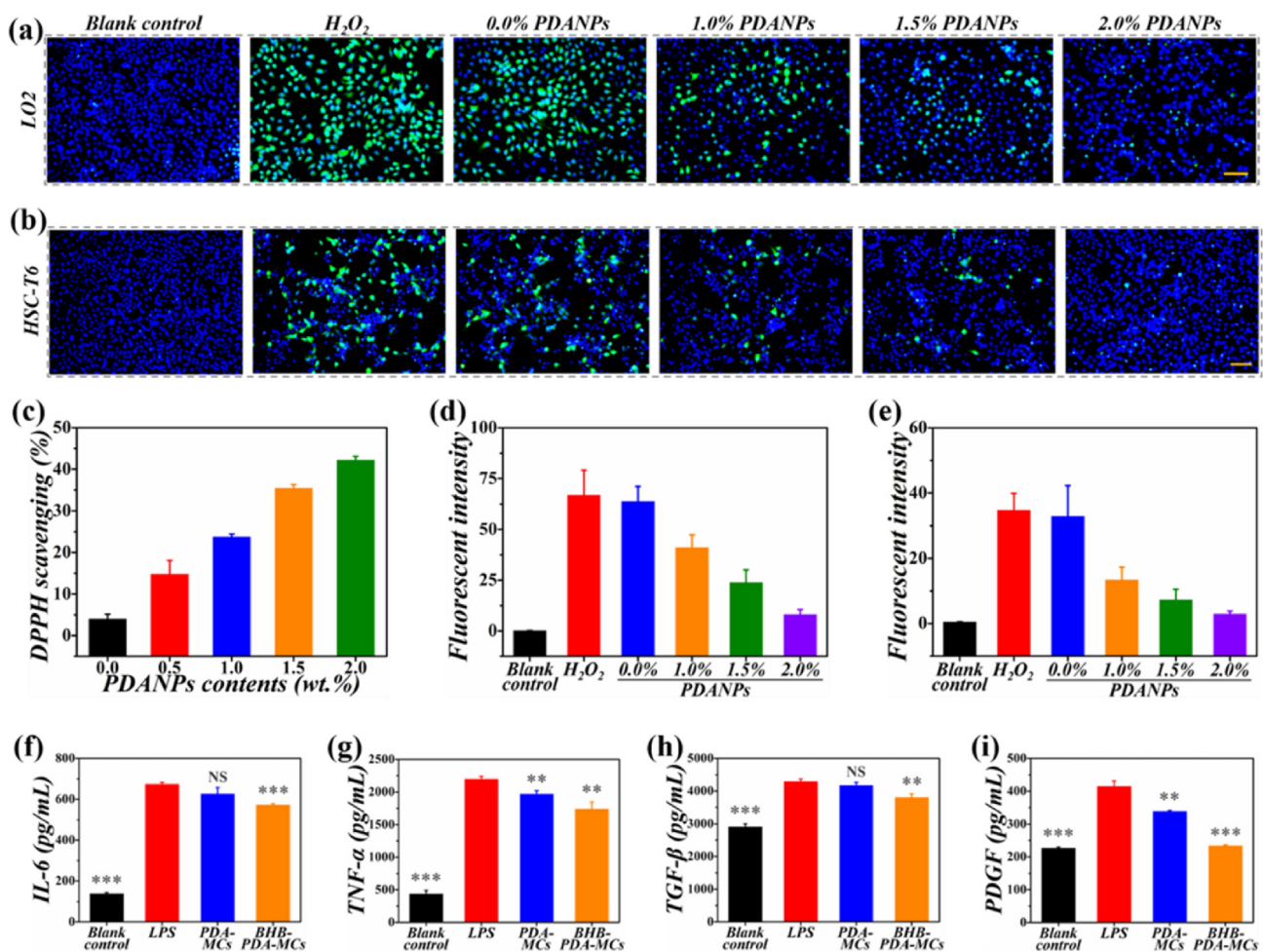

Fig. 4. a) Fluorescent images showing the ROS levels in LO2 cells after co-cultured with blank control, H_2O_2, or PDA-MCs containing 0.0%, 1.0%, 1.5%, or 2.0% PDANPs. b) Fluorescent images showing the ROS levels in HSC-T6 cells after co-cultured with blank control, H_2O_2, or PDA-MCs containing 0.0%, 1.0%, 1.5%, or 2.0% PDANPs. c) Quantitative analysis showing the DPPH scavenging ability of PDA-MCs containing different contents of PDANPs. d) Quantitative analysis showing the ability of PDA-MCs to relieve the oxidative levels in LO2 cells induced by H_2O_2. e) Quantitative analysis showing the ability of PDA-MCs to relieve the oxidative levels in HSC-T6 cells induced by H_2O_2. f-i) ELISA assay of IL-6 (f), TNF-α (g), TGF-β (h), and PDGF (i) in Raw264.7 cells after co-cultured with blank control, LPS, PDA-MCs, or BHB-PDA-MCs. Error bars represented standard deviations. **p < 0.01, ***p < 0.001, NS not significant versus LPS group. The scale bars were 50 μm.

levels in hepatocytes (LO2 cells) and HSCs (HSC-T6 cells) was investigated by intracellular ROS indicator DCFH-DA (Fig. 4a, b and S9, 10). As expected, the number of green fluorescence labeled LO2 cells and HSC-T6 cells were extremely increased after H_2O_2 stimulation, indicating significant elevations of intracellular ROS levels compared to blank control. In contrast, with the treatment of PDA-MCs, the green fluorescence attenuated gradually, and almost no fluorescent signals could be detected in both LO2 cells and HSC-T6 cells treated with microcapsules containing 2.0% PDANPs. The results of statistical analysis (Fig. 4d and e) also demonstrated that PDANPs incorporated into the polymer shell of microcapsules could reduce the H_2O_2-induced intracellular ROS levels in a dose-dependent manner. These results suggested that the ROS elimination ability of PDA-MCs could reduce the intracellular levels of oxidative stress and might play a positive role in HF management.

Evidences from clinical and animal experiments have demonstrated that macrophage accumulation is a prominent feature of chronic liver diseases upon injury changing tissue microenvironment. This accumulation results from the local proliferation of liver-resident sources or the recruitment of bone marrow-derived circulating monocytes. These accumulated macrophages are critical for HSCs activation via the production of pro-inflammatory and pro-fibrotic factors. Therefore, strategies that govern the inflammatory status of macrophages and subsequent interaction with HSCs will probably inform novel therapeutic methods for HF. Here, in vitro stimulation of Raw264.7 cells by lipopolysaccharide (LPS) increased the expression of pro-inflammatory factors, interleukin-6 (IL-6) and tumor necrosis factor-α (TNF-α), as well as pro-fibrotic factors, transforming growth factor-β (TGF-β) and platelet-derived growth factor (PDGF) (Fig. 4f–i). Although not significant, the antioxidative effects of PDA-MCs played a certain role in inhibiting the release of these bioactive factors. Notably, BHB-PDA-MCs led to significant reductions of IL-6 by 15.13%, TNF-α by 20.91%, TGF-β by 11.34%, and PDGF by 43.59%, when compared with LPS group. Previous studies have demonstrated that BHB can switch the inflammatory status of macrophages by inhibiting NLRP3 inflammasome [16]. Our study further confirmed that BHB-PDA-MCs could break the cross-talk between macrophages and HSCs by reducing the production of pro-inflammatory and pro-fibrotic factors, thus achieving an anti-fibrotic effect.

The therapeutic effects of BHB-PDA-MCs on HF development was next examined in a mouse model of CCl4-induced chronic liver damage, which exhibited considerable fidelity to the fibrotic change in human liver. The experimental arrangement was illustrated in Fig. S11. Compared to the healthy mice injected with oil, the fibrotic mice injected with CCl4 showed a poor living status and slow weight gain (Fig. S12). Interestingly, the fibrotic mice treated with PDA-MCs or BHB-PDA-MCs gradually restored their weight gain. At the end of experiment, the weight gain of BHB-PDA-MCs treated fibrotic mice was normalized up to the reference level of healthy mice. The excised livers from different treatment groups were then subjected to macroscopic analysis and weighed. As shown in Fig. 5a, the livers from healthy mice had a reddish, moist, and smooth surface with a soft texture, while the livers from fibrotic mice had a bloodless, irregular, and rough surface with an increased rigidity. Encouragingly, BHB-PDA-MCs treatment enhanced the recovery of CCl4-induced abnormalities in liver, as it had a nearly normal appearance. Consistent with the results of gross observations, the liver index (liver-to-body weight ratio) was also elevated in fibrotic mice abnormally, because of the swelling of damaged liver tissues (Fig. 5f). In contrast, PDA-MCs or BHB-PDA-MCs treatment could prevent the increase of liver index, with BHB-PDA-MCs restoring the indicator to basically normal levels. As important biomarkers of liver function, the serum levels of alanine aminotransferase (ALT) and aspartate aminotransferase (AST) were dramatically upregulated in fibrotic mice, indicating the severe hepatotoxicity exerted by repeated CCl4 injection (Fig. 5g and Fig. S13). After treatment with PDA-MCs or BHB-PDA-MCs, the elevated ALT and AST activities were remitted in different degrees. Of note, BHB-PDA-MCs treatment obtained a significantly better effect. Together, these results demonstrated that BHB-PDA-MCs treatment was

well-tolerated by mice, and could potentially have a positive role in overcoming HF-mediated morphological and functional abnormalities.

Subsequently, the histological alterations of fibrotic livers in response to BHB-PDA-MCs treatment were evaluated. As shown in Fig. 5b, the H&E-stained liver sections from healthy mice displayed a classic hexagonal structure with hepatocytes radiating outwards from a central vein and hepatic sinusoids travelling between the strips of hepatocytes. As expected, repeated CCl4 injection induced a severe disorganization of the lobular and sinusoidal structure, as well as necrotic areas formation, ballooning degeneration, and extensive neutrophil infiltration. Although no significant improvement was observed in the liver sections from PDA-MCs treated fibrotic mice, BHB-PDA-MCs treatment exhibited a more normal histological structure with fewer degenerated hepatocytes and inflammatory cell infiltration. As HF is characterized by collagen overproduction and irregular deposition, Sirius Red and Masson staining were performed to examine the liver sections in this experiment (Fig. 5c and d). For healthy mice, only thin layers of collagen fibers surrounded the portal tracts and central veins were stained. As expected, repeated CCl4 injection showed extensive fibrosis indicated by widespread red (Sirius Red) and blue (Masson) stained collagens, along with the formation of bridging fibrotic septum between adjacent vascular structures, portal to portal as well as portal to central areas. In Contrast, less collagen deposition was observed in the PDA-MCs or BHB-PDA-MCs treated fibrotic mice. Importantly, only focal marginal staining was observed in the fibrotic livers treated with BHB-PDA-MCs. The quantitative analysis in Fig. 5h, i showed that PDA-MCs treatment decreased the fibrotic area by 26.78% in Sirius Red-stained sections and 20.47% in Masson-stained sections. Strikingly, BHB-PDA-MCs treatment decreased the fibrotic area by 72.21% and 61.19% in Sirius Red- and Masson-stained sections, respectively. Collectively, these results demonstrated that BHB-PDA-MCs treatment could attenuate HF development by protecting hepatocytes and inhibiting collagen deposition.

HSCs activation is now well established as a central driver of HF. In normal liver, HSCs reside in the subendothelial space of Disse, maintain a non-proliferative and quiescent phenotype. Under chronic inflammatory environment, HSCs upregulate the expression of α-SMA, activate into proliferative, migratory, and contractile myofibroblasts, and secrete ECM molecules that accumulate and form fibrotic tissues in the liver [25]. To investigate the inhibitory effect of BHB-PDA-MCs on HSCs activation, the expression level of α-SMA was measured by immunohistochemical staining. As shown in Fig. 5e, only sporadic positive cells around the wall of central veins and blood vessels of portal tracts were observed in the healthy livers. As expected, the fibrotic livers exhibited tremendously higher numbers of positive cells in the portal tracts and connective tissue septa between hepatic lobules. In contrast, BHB-PDA-MCs treatment, not PDA-MCs treatment, significantly decreased the number of positive cells in fibrotic livers. Accordingly, the quantitative analysis also revealed that BHB-PDA-MCs treatment suppressed α-SMA expression of fibrotic livers up to 45% compared to the saline treatment (Fig. 5j). The measurement of liver hydroxyproline content, a main component of ECM collagens secreted by activated HSCs, showed a similar result (Fig. 5k). The increase of hydroxyproline level induced by repeated CCl4 injection was reduced after PDA-MCs or BHB-PDA-MCs treatment, with BHB-PDA-MCs exerting a more powerful effect. Together, these results demonstrated that BHB-PDA-MCs could promote HF regression in vivo by inhibiting HSCs activation and secretion.

In the final set of this experiment, the mechanisms of BHB-PDA-MCs in the treatment of HF was attempted to elucidate. Evidences have suggested that the chronic inflammation, triggered by a series of intrahepatic and extrahepatic events, is a prerequisite for HF development [26]. Indeed, damage-associated molecular patterns (DAMPs) released by the dying hepatocytes and pathogen-associated molecular patterns (PAMPs) derived from the gut microbiota can be recognized by the innate immune cells in liver, leading to the overwhelming release of inflammatory chemokines and cytokines. On the other hand, leukocytes recruited from the adaptive immune system also play an important role in amplifying
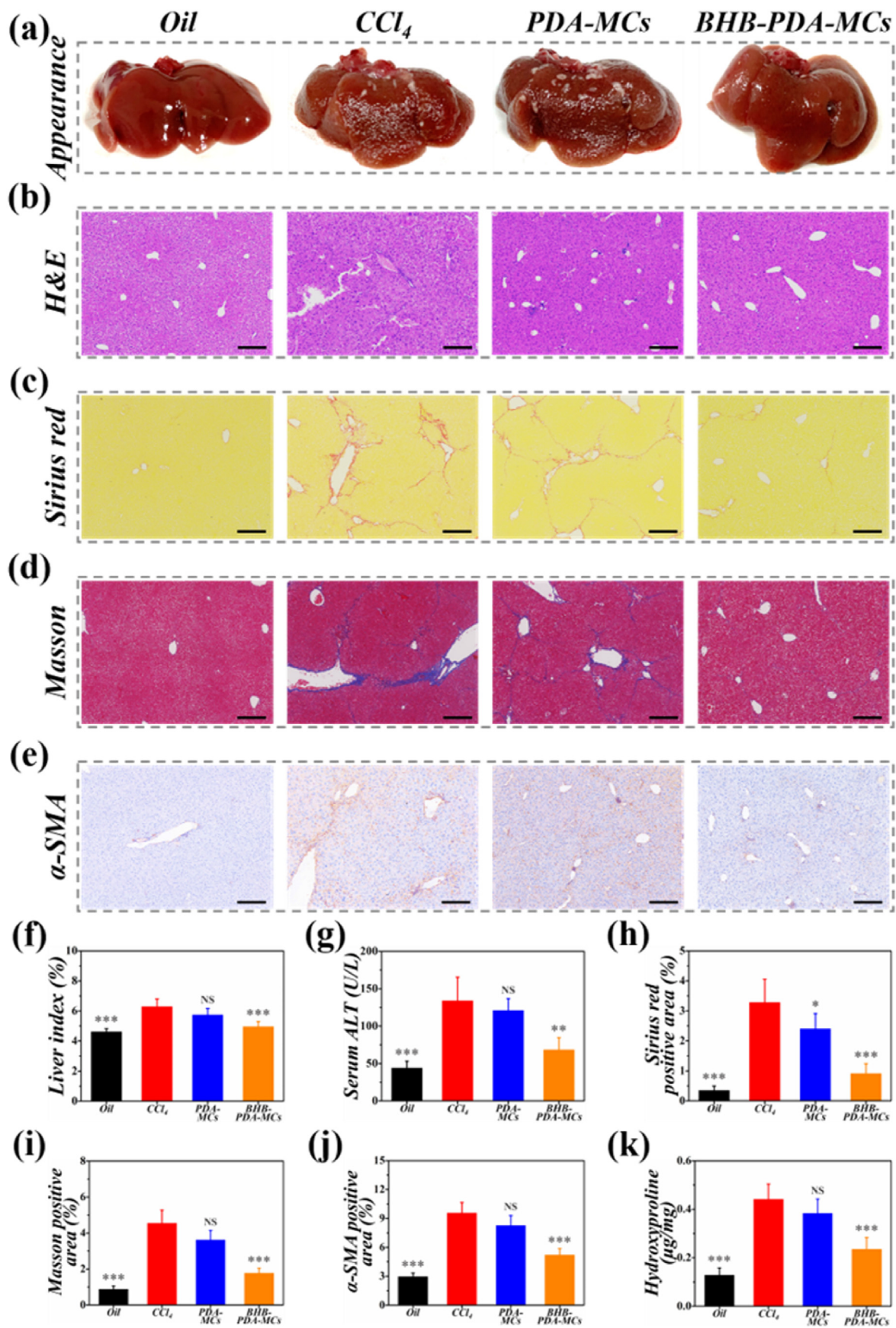
(caption on next page)

Fig. 5. a) Representative photos of liver appearance from healthy mice or fibrotic mice receiving various treatments. b) Representative photos of H&E-stained liver sections from different groups. c) Representative photos of Sirius Red-stained liver sections from different groups. d) Representative photos of Masson-stained liver sections from different groups. e) α-SMA immunohistochemical staining of liver sections from different groups. f) Quantitative analysis of the liver index. g) Serum levels of ALT from different groups. h) Quantitative analysis of collagen area stained by Sirius Red. i) Quantitative analysis of collagen area stained by Masson. j) Quantitative analysis of a-SMA positive areas. k) Measurements of liver hydroxyproline content from different groups. Error bars represented standard deviations. *p < 0.05, **p < 0.01, ***p < 0.001, NS not significant versus CCl$_4$ group. The scale bars were 200 μm. (For interpretation of the references to colour in this figure legend, the reader is referred to the Web version of this article.)
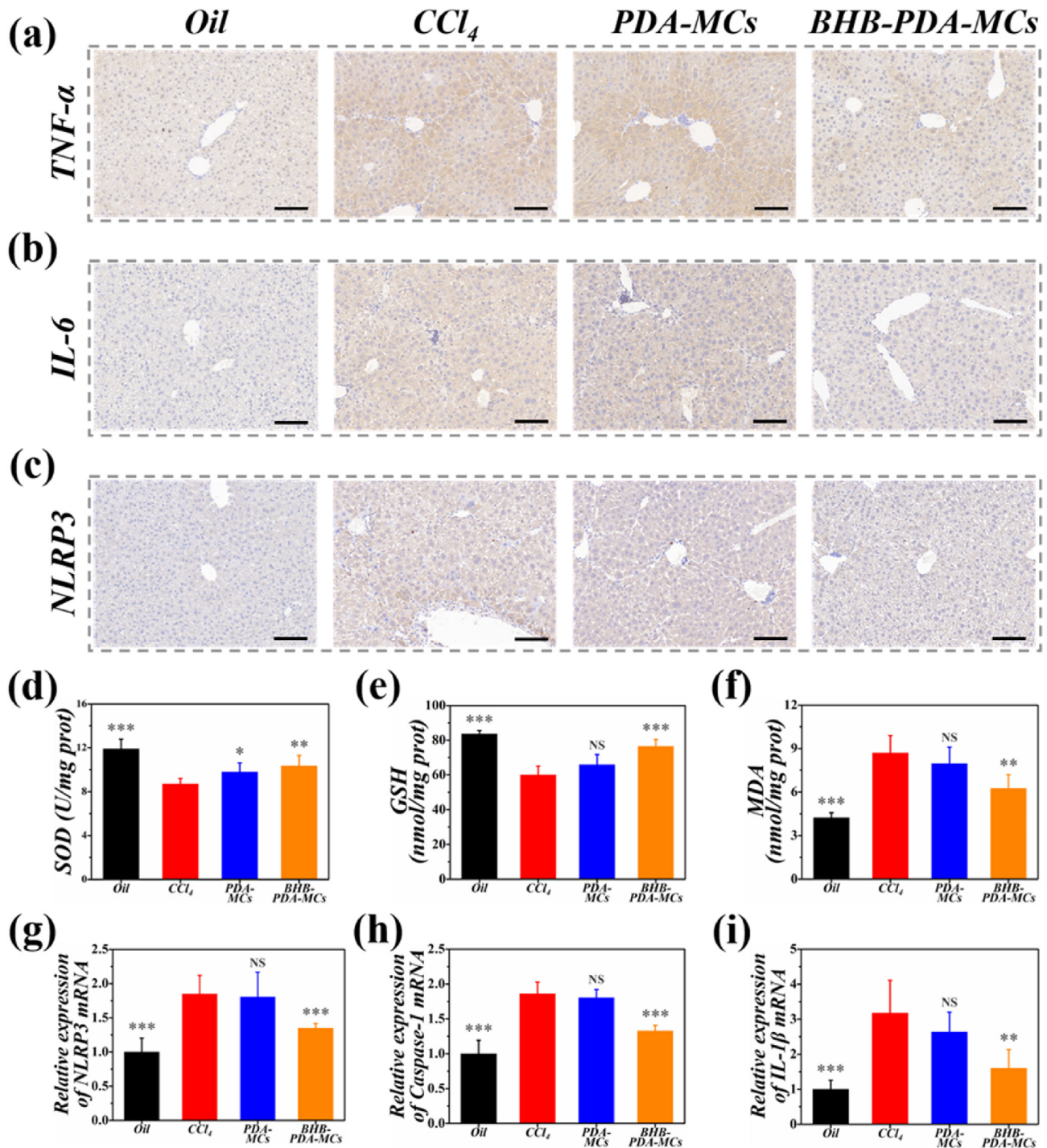

Fig. 6. a) TNF-α immunohistochemical staining of liver sections from healthy mice or fibrotic mice receiving various treatments. b) IL-6 immunohistochemical staining of liver sections from different groups. c) NLRP3 immunohistochemical staining of liver sections from different groups. d) Measurements of liver SOD activity from different groups. e) Measurements of liver GSH activity from different groups. f) Measurements of liver MDA concentration from different groups. g) Hepatic expression of NLRP3 mRNA quantified by qPCR. h) Hepatic expression of Caspase-1 mRNA quantified by qPCR. i) Hepatic expression of IL-1β mRNA quantified by qPCR. Error bars represented standard deviations. *p < 0.05, **p < 0.01, ***p < 0.001, NS not significant versus CCl$_4$ group. The scale bars were 100 μm.

inflammatory responses. In turn, the persistence of inflammatory activity contributes to the hepatocellular injury and death, creating a feed-forward loop between liver injury and inflammation [1]. In this regard, the expression profiles of TNF-α and IL-6 were measured to investigate the role of BHB-PDA-MCs in alleviating chronic inflammation. For healthy livers, the immunohistochemical staining from Fig. 6a, **b** showed few signs of inflammatory responses, as only a small amount of cytokines secretion was found. Conversely, the fibrotic livers were found to exhibit a severe inflammatory response associated with extensive positive areas of TNF-α and IL-6. Although PDA-MCs treatment did not change the staining results, BHB-PDA-MCs treatment led to a marked reduction in the expression levels of TNF-α and IL-6, indicating an excellent anti-inflammatory performance.

Oxidative stress has also been implicated in HF development. In normal livers, the generation and elimination of ROS maintain balanced with the help of endogenous antioxidants, such as superoxide dismutase (SOD) and glutathione (GSH). However, multiple simultaneous triggers during HF development including inflammatory responses, cell death pathways, mitochondrial dysfunction, and endoplasmic reticulum stress can lead to ROS overproduction, exceeding the normal elimination mechanisms. As a result, the lipid peroxidation products, such as malondialdehyde (MDA), not only act as DAMPs in promoting inflammatory responses, but also provide direct activation signals for HSCs to drive HF progression [27]. In this study, repeated CCl_4 injection induced oxidative stress and lipid peroxidation in the liver, with significantly lower SOD and GSH activities, as well as higher MDA concentration (Fig. 6d–f). However, the activities of SOD and GSH, and the concentration of MDA in fibrotic livers were normalized with the treatment of PDA-MCs or BHB-PDA-MCs. Obviously, the normalized potency of BHB-PDA-MCs on these indicators of oxidative stress was significantly stronger than PDA-MCs. Collectively, these results indicated that BHB-PDA-MCs had a powerful ability to rescue the hepatocellular anti-oxidant system and alleviate the oxidative stress in livers.

Abnormal activation of the NLRP3 inflammasome have been found to serve as an important contributor to chronic inflammation and subsequent fibrotic disorders. Upon stimulation, components of the NLRP3 inflammasome are recruited and assembled, leading to cleavage of pro-Caspase-1 into its active form, which then cleaves pro-IL-1β and pro-IL-18 into their mature forms. These NLRP3 inflammasome mediated cytokines are pro-fibrotic, critical for HSCs activation, and associated with HF development [28]. As shown in Fig. 6c, the expression level of NLRP3 in healthy livers was very low, while NLRP3 was significantly upregulated after repeated CCl_4 injection, in correlation with fibrosis progression. Therefore, more and more evidences have suggested that targeting the NLRP3 inflammasome provides a potential therapeutic strategy for fibrosis management [8]. Recent studies have reported that BHB plays an immunomodulatory role by inhibiting the NLRP3 inflammasome activation, and exogenous supplement of BHB has protective functions in NLRP3 inflammasome mediated diseases [14–16]. All these striking researches raised the question that whether the beneficial effect of BHB-PDA-MCs in relieving HF was also related to the blockade of NLRP3-Caspase-1-IL-1β pathway. As shown in Fig. 6c, the expression level of NLRP3 in fibrotic livers was reduced by BHB-PDA-MCs treatment, while PDA-MCs treatment exhibited no obvious inhibiting effects. Accordingly, the results of quantitative polymerase chain reaction (qPCR) analysis also showed that BHB-PDA-MCs treatment, not PDA-MCs treatment, suppressed the expression levels of NLRP3, Caspase-1, and IL-1β in fibrotic livers, in comparison to the saline treatment (Fig. 6g–i). Together, these results demonstrated that the controlled BHB delivery from BHB-PDA-MCs could inhibit NLRP3 inflammasome activation in vivo and contribute to the protective effect of BHB-PDA-MCs against HF development.

3. Conclusion

In conclusion, BHB-PDA-MCs were successfully constructed by

microfluidics in this study for HF management. Benefited from the powerful droplet manipulation capability of microfluidics, the resultant microcapsules had a desired core-shell structure and narrow size distribution. Taking advantage of the microencapsulation technology, substantial amounts of drug molecules could be loaded into BHB-PDA-MCs, retaining their biological activity, and delivered in a controlled manner to prolong their in vivo retention time. Meanwhile, with addition of PDANPs in the polymer shell of BHB-PDA-MCs, the resultant microcapsules had a broad-spectrum antioxidative property, reducing the intracellular levels of oxidative stress. Importantly, in a mouse model of CCl_4-induced HF, BHB-PDA-MCs could inhibit HSCs activation, decrease collagen deposition, relieve pathological changes, and protect liver functions. Further mechanistic studies revealed that the fibrotic mice treated with BHB-PDA-MCs exhibited a low level of inflammatory response and oxidative stress, which might be related to the BHB-mediated NLRP3 inflammasome inactivation and PDANPs-mediated free radical scavenging. Collectively, all these results manifested that BHB-PDA-MCs would be a promising therapeutic platform and open a new avenue for HF management.

4. Materials and methods

4.1. Materials

Dopamine hydrochloride, PVA (Mw 13000–23000, 87–89% hydrolyzed), PLGA (lactide: glycolide = 50 : 50, ester terminated, average Mw 100000), BHB, DOX, DPPH, and LPS (from *Escherichia coli* O55: B5) were obtained from Sigma-Aldrich (St. Louis, MO, USA). DCM, sodium hydroxide (NaOH), CCl_4, and olive oil was obtained from Sinopharm Chemical Reagent (Shanghai, China). RPMI-1640 medium, Dulbecco's modified Eagle medium (DMEM, high glucose), fetal bovine serum (FBS), PBS, and penicillin and streptomycin were obtained from Gibco/Life-Technologies (Beijing, China). FITC and Hoechst 33342 were obtained from Solarbio (Beijing, China). DCFH-DA was obtained from AbMole Bioscience (Houston, TX, USA). Mouse ELISA kits for IL-6, TNF-α, TGF-β, and PDGF were obtained from Signalway Antibody (Greenbelt, MD, USA). Assay kits for hydroxyproline, SOD, GSH, and MDA were obtained from Nanjing Jiancheng Bioengineering Institute (Nanjing, China). The primary antibodies for α-SMA, TNF-α, IL-6, and NLRP3 were obtained from Abcam (Waltham, MA, USA). LO2, HSC-T6, and Raw264.7 cells were obtained from the Cell Bank of Chinese Academy of Sciences (Shanghai, China). Deionized water was used in all experiments. All other chemical reagents were of the best grade available and used as received.

4.2. PDANPs preparation

PDANPs were synthesized by a conventional self-polymerization method. Briefly, 90 mg dopamine was dissolved in 45 mL deionized water, then 0.38 mL of 1 M NaOH solution was added. After reaction for 12 h, PDANPs were collected by centrifugation (14800 rpm, 10min) and washed with deionized water for three times. The structure of PDANPs was observed by TEM (JEOL JEM2100). ^{1}H NMR spectrum of dopamine monomer and PDANPs dissolved in D_2O were investigated using Bruker Ultrashield 400 Plus to detect the characteristic proton signals.

4.3. BHB-PDA-MCs fabrication

Three round microcapillaries (inner, middle, and outer) were nested coaxially within a square microcapillary on a glass slide for the construction of microfluidic device, and all these microcapillaries were obtained from World Precision Instruments, Inc. The inner microcapillary was heated and stretched using a gas burner to reach a tapered orifice of about 40 μm diameter. The middle microcapillary was pulled by a micropipette puller (Sutter P97) and sanded by hand to reach a tapered orifice of about 200 μm diameter. These microcapillaries were

appropriately assembled and sealed by dispensing needles and epoxy resin adhesives where necessary. The inner aqueous phase was 10 mg/mL BHB dissolved in deionized water and pumped into the inner microcapillary. The middle oil phase was DCM solution of 120 mg/mL PLGA, in which 1.8 mg/mL PDANPs were dispersed, and pumped into the interstice between the inner and middle microcapillary. The outer aqueous phase was 20 mg/mL PVA dissolved in deionized water and pumped into the interstice between the middle and square microcapillary. These three fluids were pumped by a syringe pump (Harvard PHD2000) and flowed in the same direction inside the microfluidic device. The real-time generation process of double emulsions was recorded using a stereomicroscope (Nikon E600) equipped with a charged coupled device (Evolution MP5.0 RTV).

Then, the collected double emulsions were put into a rotary evaporator (IKA RV10). After DCM evaporation at room temperature for 24 h, the solidified BHB-PDA-MCs were collected and washed with deionized water for three times. Both the double emulsions and resultant microcapsules were observed using an optical microscope (Olympus MVX10), and the diameters were measured using AOS Imaging Studio software. After freeze-drying and spraying gold on BHB-PDA-MCs, the detailed structural characteristics were investigated using SEM (Hitachi S3000 N). To observe the drug storage in BHB-PDA-MCs, 1 mg/mL FITC with green fluorescence, instead of BHB, was loaded into PDA-MCs. Fluorescent cross-sectional images were captured using a confocal microscope (Olympus FV10i), taken in the z-direction from the top of microcapsules to the bottom.

4.4. Drug loading and release assay

To investigate the effect of PLGA concentration used during FITC-PDA-MCs fabrication on the drug loading efficiency of resultant microcapsules, FITC-PDA-MCs fabricated from 100 mg/mL, 120 mg/mL, and 150 mg/mL PLGA solution were grinded completely in PBS solution to release all the encapsulated FITC. After filtration, the FITC content in supernatant was measured using a microplate reader (BioTek Synergy H1) at 490 nm wavelength. The drug encapsulation efficiency was calculated by the following equation: Encapsulation efficiency (%) = encapsulated amount of FITC/initial amount of FITC × 100%. The drug loading content was calculated by the following equation: Loading content (μg/mg) = encapsulated amount of FITC/total weight of microcapsules. To investigate the drug release performance of FITC-PDA-MCs, certain amount of microcapsules were immersed into 1 mL PBS solution and incubated in a shaking water bath at 37 °C. At predetermined timepoints, 100 μL PBS solution was collected and refreshed with the same volume of fresh PBS solution. The content of released FITC in collected PBS solution was measured using a microplate reader. All the data were averaged from three parallel experiments.

4.5. In vivo retention time

Nude mice with 5–6 weeks old were divided into two groups (n = 3 in each group). For DOX group, the mice were intraperitoneally injected with 1 mg/kg free DOX dissolved in saline solution. For DOX-PDA-MCs group, the mice were intraperitoneally injected with DOX-PDA-MCs at the same dose of free DOX. At 2-h, 1-day, 3-day, and 7-day after injection, the mice were anesthetized using isoflurane and subjected to an in vivo imaging system (Caliper IVIS Lumina XR), using 588 nm and 650 nm excitation and emission wavelengths, respectively. The fluorescent intensity was analyzed using an in vivo imaging software (Caliper Life Sciences, CA, USA) and presented as the total radiance normalized to the initial 2-h signal. At 3-day post injection of DOX-PDA-MCs, the nude mice (n = 3) were sacrificed with their major organs collected for ex vivo fluorescent imaging.

4.6. In vitro antioxidative assay

The antioxidative activities of PDA-MCs with increasing PDA contents were evaluated by determining their capacities to scavenge DPPH free radicals. Briefly, 1.0 mg PDA-MCs were immersed into 100 μM DPPH solution of water and methanol (V_{water}: $V_{methanol}$ = 1 : 1, 1.0 mL) and incubated in a dark environment for 30min. Then, optical absorbance (OD) value of the mixture was determined at 517 nm wavelength using a microplate reader. The free radical scavenging efficiency was calculated by the following equation: DPPH scavenging % = (OD_{517} from blank control – OD_{517} from test sample)/OD_{517} from blank control × 100%.

4.7. Cell experiments

LO2 cells were cultured in RPMI-1640 medium, while HSC-T6 and Raw264.7 cells cultured in DMEM medium. All these mediums were supplemented with 10% FBS and 1% penicillin-streptomycin, maintained at 37 °C in a humidified 5% CO_2 environment. The cell-permeable DCFH-DA fluorescent probe was used to detect the ROS levels in LO2 and HSC-T6 cells. The cells were seeded in 6-well plates with a density of 3×10^5 per well, and treated with PDA-MCs containing 0.0%, 1.0%, 1.5%, or 2.0% PDANPs for 24 h. Then, the culture medium was discarded and the cells were incubated with fresh medium containing 300 μM H_2O_2 for 6 h. After PBS washing three times, a final concentration of 10 μM DCFH-DA was added to each well and incubated for 30min at 37 °C. The cells without any treatment were defined as blank control, and the fluorescent images were visualized by an inverted microscope (Zeiss Axio Observer Z1) before staining the nuclei with Hoechst for 10min. The fluorescent signal intensity was quantified via ImageJ software. Raw264.7 macrophages cultured in 6-well plates were classified into four groups: 1) Blank control: Cells cultured without any treatments; 2) LPS group: Cells cultured with 200 ng/mL LPS; 3) PDA-MCs group: Cells cultured with 100 mg/mL PDA-MCs and 200 ng/mL LPS; 4) BHB-PDA-MCs group: Cells cultured with 100 mg/mL BHB-PDA-MCs and 200 ng/mL LPS. After treated for 24 h, the cell culture supernatants from each group were collected for quantifying the following cytokines using ELISA kits: IL-6, TNF-α, TGF-β, and PDGF according to the manufacturer's recommendations. All the experiments were repeated three times.

4.8. Animal experiments

Male C57BL/6J mice with 6–8 weeks old were purchased from the Experimental Animal Center of Soochow University (Suzhou, China). Three mice per cage were housed in a 12 h light/12 h dark cycle, with free access to food and water. After one week of acclimatization, these mice were randomly divided into normal group (n = 6) and fibrotic group (n = 18). For fibrotic group, mice were intraperitoneally administrated with CCl_4 (25% in olive oil) two times a week for six weeks to induce and maintain HF, at a bolus dose of 2 μL/g body weight. For normal group, mice were intraperitoneally administrated with olive oil alone. All animal experiments were performed in accordance with protocols approved by the Animal Welfare and Ethics Committee of Soochow University (Suzhou, China, Grant No. 202207A0910).

Before the last four administration of CCl_4, the mice in fibrotic group were further divided into three groups (n = 6 in each group). For saline group, 500 μL normal saline was administrated to the fibrotic mice by intraperitoneal injection. For PDA-MCs group, 500 mg PDA-MCs dispersed in 500 μL saline was administrated to the fibrotic mice by intraperitoneal injection. For BHB-PDA-MCs group, 500 mg BHB-PDA-MCs dispersed in 500 μL saline was administrated to the fibrotic mice by intraperitoneal injection. Body weight of all groups was measured at defined time intervals using a digital balance. At 72 h after the last CCl_4 injection, all mice were euthanized by exsanguination after ketamine and

xylazine anesthesia. The blood samples and liver tissues were collected for further analysis.

After blood collection from the ophthalmic veins of mice in each group, the serum sample was obtained by centrifugation of the whole blood (4000 rpm, 10min). ALT and AST levels were measured using an automatic biochemical analyzer. Liver tissues from all groups were collected and weighted. One part of liver fragments was frozen at −80 °C for collagen content evaluation, oxidative stress analysis, and qPCR quantification. Another part of liver fragments was fixed in formalin, dehydrated, embedded in paraffin, and sectioned into 4 μm sections. The tissue sections were then stained with H&E, Masson, and Sirius Red following the routing protocols in pathology laboratory. The positive areas of Masson and Sirius Red stained images were analyzed quantitatively using Image J software.

For evaluating the collagen content of liver tissues, the hydroxyproline level in each sample was measured using the Hydroxyproline Assay Kit and normalized to the liver tissue weight according to the manufacturer's protocol. For evaluating the oxidative stress of liver tissue, the production levels of SOD, GSH, and MDA were measured following the protocol provided by manufacturer. For immunohistochemistry staining, after routine deparaffinization, rehydration, endogenous peroxidase blockage, and heat-induced antigen retrieval, the liver sections were incubated with primary antibodies against α-SMA (1:100), TNF-α (1:200), IL-6 (1:200), and NLRP3 (1:100). Finally, the sections were incubated with secondary antibodies and diaminobenzidine, and visualized under optical microscope. The quantification of positively stained areas was performed using Image J software. For qPCR, total RNA was isolated from homogenized tissues using Triquick reagent (Servicebio, China), and 1 μg of total RNA was reverse-transcribed into complementary DNA (cDNA) using First Strand cDNA Synthesis Kit (Servicebio, China). The resulting cDNAs were amplified using 2 × SYBR Green qPCR Master Mix (Servicebio, China) and CFX96 real-time PCR system (Bio-Rad, USA). The relative expression of target genes was normalized by GAPDH expression as an internal control. PCR primer sequences were listed in Table S1.

4.9. Statistical analysis

All data were expressed as means ± standard deviation (SD). Differences between multiple groups were compared using one-way analysis of variance (ANOVA) with Tukey test. All analyses were performed using Graphpad Prism 7.0 (GraphPad Software, CA, USA), and $p < 0.05$ was considered statistically significant.

Credit author statement

Xin Zhao: Methodology, Validation, Formal analysis, Investigation, Writing – original draft; **Zun Fan:** Methodology, Validation, Formal analysis, Investigation; **Chengyang Zhu:** Methodology, Validation, Formal analysis, Investigation; **Weigang Zhang:** Conceptualization, Writing – review & editing, Supervision; **Lei Qin:** Conceptualization, Writing – review & editing, Supervision.

Declaration of competing interest

The authors declare that they have no known competing financial interests or personal relationships that could have appeared to influence the work reported in this paper.

Data availability

Data will be made available on request.

Acknowledgements

Appendix A. Supplementary data

Supplementary data to this article can be found online at https://doi.org/10.1016/j.mtbio.2023.100711.

References

[1] T. Kisseleva, D. Brenner, Molecular and cellular mechanisms of liver fibrosis and its regression, Nat. Rev. Gastroenterol. Hepatol. 18 (2021) 151–166.
[2] S.L. Friedman, M. Pinzani, Hepatic fibrosis 2022: unmet needs and a blueprint for the future, Hepatology 75 (2022) 473–488.
[3] P. Ginès, A. Krag, J.G. Abraldes, E. Solà, N. Fabrellas, P.S. Kamath, Liver cirrhosis, Lancet 398 (2021) 1359–1376.
[4] G.N. Ioannou, Epidemiology and risk-stratification of NAFLD-associated HCC, J. Hepatol. 75 (2021) 1476–1484.
[5] N.C. Henderson, F. Rieder, T.A. Wynn, Fibrosis: from mechanisms to medicines, Nature 587 (2020) 555–566.
[6] X. Zhao, J.Y.Y. Kwan, K. Yip, P.P. Liu, F.F. Liu, Targeting metabolic dysregulation for fibrosis therapy, Nat. Rev. Drug Discov. 19 (2020) 57–75.
[7] P. Trivedi, S. Wang, S.L. Friedman, The power of plasticity-metabolic regulation of hepatic stellate cells, Cell Metabol. 33 (2021) 242–257.
[8] S. Gaul, A. Leszczynska, F. Alegre, B. Kaufmann, C.D. Johnson, L.A. Adams, A. Wree, G. Damm, D. Seehofer, C.J. Calvente, D. Povero, T. Kisseleva, A. Eguchi, M.D. McGeough, H.M. Hoffman, P. Pelegrin, U. Laufs, A.E. Feldstein, Hepatocyte pyroptosis and release of inflammasome particles induce stellate cell activation and liver fibrosis, J. Hepatol. 74 (2021) 156–167.
[9] S. Schuster, D. Cabrera, M. Arrese, A.E. Feldstein, Triggering and resolution of inflammation in NASH, Nat. Rev. Gastroenterol. Hepatol. 15 (2018) 349–364.
[10] G. Targher, K.E. Corey, C.D. Byrne, M. Roden, The complex link between NAFLD and type 2 diabetes mellitus - mechanisms and treatments, Nat. Rev. Gastroenterol. Hepatol. 18 (2021) 599–612.
[11] A.K. Singal, P. Mathurin, Diagnosis and treatment of alcohol-associated liver disease: a review, JAMA 326 (2021) 165–176.
[12] R.F. Schwabe, I. Tabas, U.B. Pajvani, Mechanisms of fibrosis development in nonalcoholic steatohepatitis, Gastroenterology 158 (2020) 1913–1928.
[13] A. Wang, H.H. Luan, R. Medzhitov, An evolutionary perspective on immunometabolism, Science 363 (2019) eaar3932.
[14] O. Dmitrieva-Posocco, A.C. Wong, P. Lundgren, A.M. Golos, H.C. Descamps, L. Dohnalová, Z. Cramer, Y. Tian, B. Yueh, O. Eskiocak, G. Egervari, Y. Lan, J. Liu, J. Fan, J. Kim, B. Madhu, K.M. Schneider, S. Khoziainova, N. Andreeva, Q. Wang, N. Li, E.E. Furth, W. Bailis, J.R. Kelsen, K.E. Hamilton, K.H. Kaestner, S.L. Berger, J.A. Epstein, R. Jain, M. Li, S. Beyaz, C.J. Lengner, B.W. Katona, S.I. Grivennikov, C.A. Thaiss, M. Levy, β-Hydroxybutyrate suppresses colorectal cancer, Nature 605 (2022) 160–165.
[15] R. Nielsen, N. Møller, L.C. Gormsen, L.P. Tolbod, N.H. Hansson, J. Sorensen, H.J. Harms, J. Frøkiær, H. Eiskjaer, N.R. Jespersen, S. Mellemkjaer, T.R. Lassen, K. Pryds, H.E. Bøtker, H. Wiggers, Cardiovascular effects of treatment with the ketone body 3-hydroxybutyrate in chronic heart failure patients, Circulation 139 (2019) 2129–2141.
[16] Y.H. Youm, K.Y. Nguyen, R.W. Grant, E.L. Goldberg, M. Bodogai, D. Kim, D. D'Agostino, N. Planavsky, C. Lupfer, T.D. Kanneganti, S. Kang, T.L. Horvath, T.M. Fahmy, P.A. Crawford, A. Biragyn, E. Alnemri, V.D. Dixit, The ketone metabolite β-hydroxybutyrate blocks NLRP3 inflammasome-mediated inflammatory disease, Nat. Med. 21 (2015) 263–269.
[17] T. Bollhorst, K. Rezwan, M. Maas, Colloidal capsules: nano- and microcapsules with colloidal particle shells, Chem. Soc. Rev. 46 (2017) 2091–2126.
[18] X. Zhang, Q. Qu, A. Zhou, Y. Wang, J. Zhang, R. Xiong, V. Lenders, B.B. Manshian, D. Hua, S.J. Soenen, C. Huang, Core-shell microparticles: from rational engineering to diverse applications, Adv. Colloid Interface Sci. 299 (2022), 102568.
[19] P. Yang, F. Zhu, Z. Zhang, Y. Cheng, Z. Wang, Y. Li, Stimuli-responsive polydopamine-based smart materials, Chem. Soc. Rev. 50 (2021) 8319–8343.
[20] H.A. Lee, E. Park, H. Lee, Polydopamine and its derivative surface chemistry in material science: a focused review for studies at KAIST, Adv. Mater. 32 (2020), e1907505.
[21] L. Yang, Y. Liu, L. Sun, C. Zhao, G. Chen, Y. Zhao, Biomass microcapsules with stem cell encapsulation for bone repair, Nano-Micro Lett. 14 (2021) 4.
[22] J.W. Kim, S.H. Han, Y.H. Choi, W.M. Hamonangan, Y. Oh, S.H. Kim, Recent advances in the microfluidic production of functional microcapsules by multiple-emulsion templating, Lab Chip 22 (2022) 2259–2291.
[23] H. Kim, S.H. Lee, A. Wentworth, S. Babaee, K. Wong, J.E. Collins, J. Chu, K. Ishida, J. Kuosmanen, J. Jenkins, K. Hess, A. Lopes, J. Morimoto, Q. Wan, S.V. Potdar, R. McNally, C. Tov, N.Y. Kim, A. Hayward, D. Wollin, R. Langer, G. Traverso, Biodegradable ring-shaped implantable device for intravesical therapy of bladder disorders, Biomaterials 288 (2022), 121703.
[24] M.J. Mitchell, M.M. Billingsley, R.M. Haley, M.E. Wechsler, N.A. Peppas, R. Langer, Engineering precision nanoparticles for drug delivery, Nat. Rev. Drug Discov. 20 (2021) 101–124.
[25] P. Ramachandran, R. Dobie, J.R. Wilson-Kanamori, E.F. Dora, B.E.P. Henderson, N.T. Luu, J.R. Portman, K.P. Matchett, M. Brice, J.A. Marwick, R.S. Taylor, M. Efremova, R. Vento-Tormo, N.O. Carragher, T.J. Kendall, J.A. Fallowfield,

E.M. Harrison, D.J. Mole, S.J. Wigmore, P.N. Newsome, C.J. Weston, J.P. Iredale, F. Tacke, J.W. Pollard, C.P. Ponting, J.C. Marioni, S.A. Teichmann, N.C. Henderson, Resolving the fibrotic niche of human liver cirrhosis at single-cell level, Nature 575 (2019) 512–518.

[26] O. Krenkel, T. Puengel, O. Govaere, A.T. Abdallah, J.C. Mossanen, M. Kohlhepp, A. Liepelt, E. Lefebvre, T. Luedde, C. Hellerbrand, R. Weiskirchen, T. Longerich, I.G. Costa, Q.M. Anstee, C. Trautwein, F. Tacke, Therapeutic inhibition of inflammatory monocyte recruitment reduces steatohepatitis and liver fibrosis, Hepatology 67 (2018) 1270–1283.

[27] M. Ruart, L. Chavarria, G. Campreciós, N. Suárez-Herrera, C. Montironi, S. Guixé-Muntet, J. Bosch, S.L. Friedman, J.C. Garcia-Pagán, V. Hernández-Gea, Impaired endothelial autophagy promotes liver fibrosis by aggravating the oxidative stress response during acute liver injury, J. Hepatol. 70 (2019) 458–469.

[28] M. de Carvalho Ribeiro, G. Szabo, Role of the inflammasome in liver disease, Annu. Rev. Pathol. 17 (2022) 345–365.